

Ultrafast dynamics of excitons in black phosphorus

Geoffroy Kremer,^{1,2} Juan F. P. Mosquera,^{3,2} Joël Morf,² Aymen Mahmoudi,² Frédéric Chassot,² Viktor Christiansson,⁴ Maxime Rumo,² Manuele Balestra,⁵ Fabian O. von Rohr,⁵ Philipp Werner,² Michael Schüler,^{3,2} and Claude Monney²

¹*Université de Lorraine, CNRS, IJL, F-54000 Nancy, France*

²*Department of Physics, University of Fribourg, Chemin du Musée 3, 1700 Fribourg, Switzerland*

³*PSI Center for Scientific Computing, Theory and Data,
Paul Scherrer Institute, 5232 Villigen PSI, Switzerland*

⁴*Institute of Solid State Physics, TU Wien, Vienna, Austria*

⁵*Department of Quantum Matter Physics, University of Geneva, CH-1211 Geneva, Switzerland*

Excitons are key quasi-particles determining the optical properties of solids. As such, they can be utilized to coherently control the electronic structure of materials using optical femtosecond pulses. Identifying the decoherence mechanism during the early non-equilibrium dynamics is crucial to achieve light-induced band-structure engineering in semiconductors. Here, we generate excitons in the direct band gap semiconductor black phosphorus with a resonant mid-infrared photoexcitation. Using time- and angle-resolved photoemission spectroscopy, we track their complex ultrafast dynamics on the few-picosecond time scale. We develop a quantum-kinetic theoretical framework to model the decoherence of excitons into dark excitons via phonon scattering. By combining simulation and experiment, we quantify key parameters describing the early dynamics of the excitons. Our work highlights phonon-mediated intravalley scattering as a fundamental limitation for coherent exciton phenomena in single-valley semiconductors.

INTRODUCTION

Excitons – electron-hole pairs bound by the Coulomb interaction – govern the optical response of semiconductors and play a central role in a broad class of nonequilibrium phenomena, from light harvesting to ultrafast control [1]. Their coherent superposition states, in which the exciton wavefunction carries a well-defined quantum mechanical phase, are of particular current interest across several fields. In quantum information science, exciton coherence underpins proposals for optically addressable qubits and ultrafast all-optical logic [2]. In condensed matter physics, proposals for Floquet engineering of exciton bands, the formation of hybrid light-matter polariton states, and the optically driven control of excitonic order all rely critically on the ability to generate and sustain coherent exciton populations over timescales long enough to manipulate them [3–6]. In all of these examples, the key ingredient is the exciton coherence, and its survival is the central limiting factor.

Answering this question quantitatively has proved difficult. On the theoretical side, substantial progress has been made: excitonic absorption spectra including the linewidth due to exciton-phonon coupling can be computed [7–9], and quantum-kinetic frameworks extending the semiconductor Bloch equations to include exciton-phonon scattering are able to describe real-time exciton dynamics [10–16]. On the experimental side, however, accessing coherence dynamics directly remains a challenge: optical spectroscopies are sensitive to the macroscopic polarization and convolve population and coherence dynamics in ways that are difficult to disentangle. A direct, momentum-resolved window onto the full exciton dynamics — bright and dark states alike — is needed.

Time- and angle-resolved photoemission spectroscopy (trARPES) has emerged as a uniquely powerful tool in this

context [17]. By directly tracking the momentum-resolved distribution of photoexcited carriers as a function of pump-probe delay, trARPES grants access to exciton dynamics in ways that are complementary to and often beyond what optical spectroscopies can reveal [18–20]. Most works to date has focused on transition-metal dichalcogenides (TMDCs), where the multi-valley electronic structure introduces a rich interplay between spin, valley, and exciton degrees of freedom [19, 21–26]. In these materials, intervalley scattering — mediated by phonons or disorder — plays a dominant role in exciton relaxation and dephasing, efficiently transferring population from optically bright states at zero center-of-mass momentum to momentum-forbidden dark exciton states on femtosecond to picosecond timescales. While this physics is now relatively well characterized, the multivalley complexity also obscures more elementary mechanisms of exciton decoherence that are intrinsic to simpler, single-valley semiconductors.

Black phosphorus (BP) provides a compelling alternative platform to isolate and study these elementary processes. With a single relevant valley at the $\bar{\Gamma}$ point of a rectangular surface Brillouin zone, BP offers a unique opportunity to isolate exciton dynamics without the complications of intervalley scattering. Bulk BP hosts excitons with pronounced in-plane anisotropy, strong light-matter coupling, and a direct band gap that depends on layer thickness across the infrared to visible range [27–29]. Despite these favorable properties and growing experimental interest in its nonequilibrium response [30–33], the microscopic dynamics of coherent excitons in BP — their formation, dephasing, and conversion into dark states — have remained largely unexplored.

Here we address this gap by combining trARPES with a quantum-kinetic theoretical framework designed for quantitative comparison with the experiment. Using a tunable mid-infrared (MIR) pump laser we can selectively excite excitons,

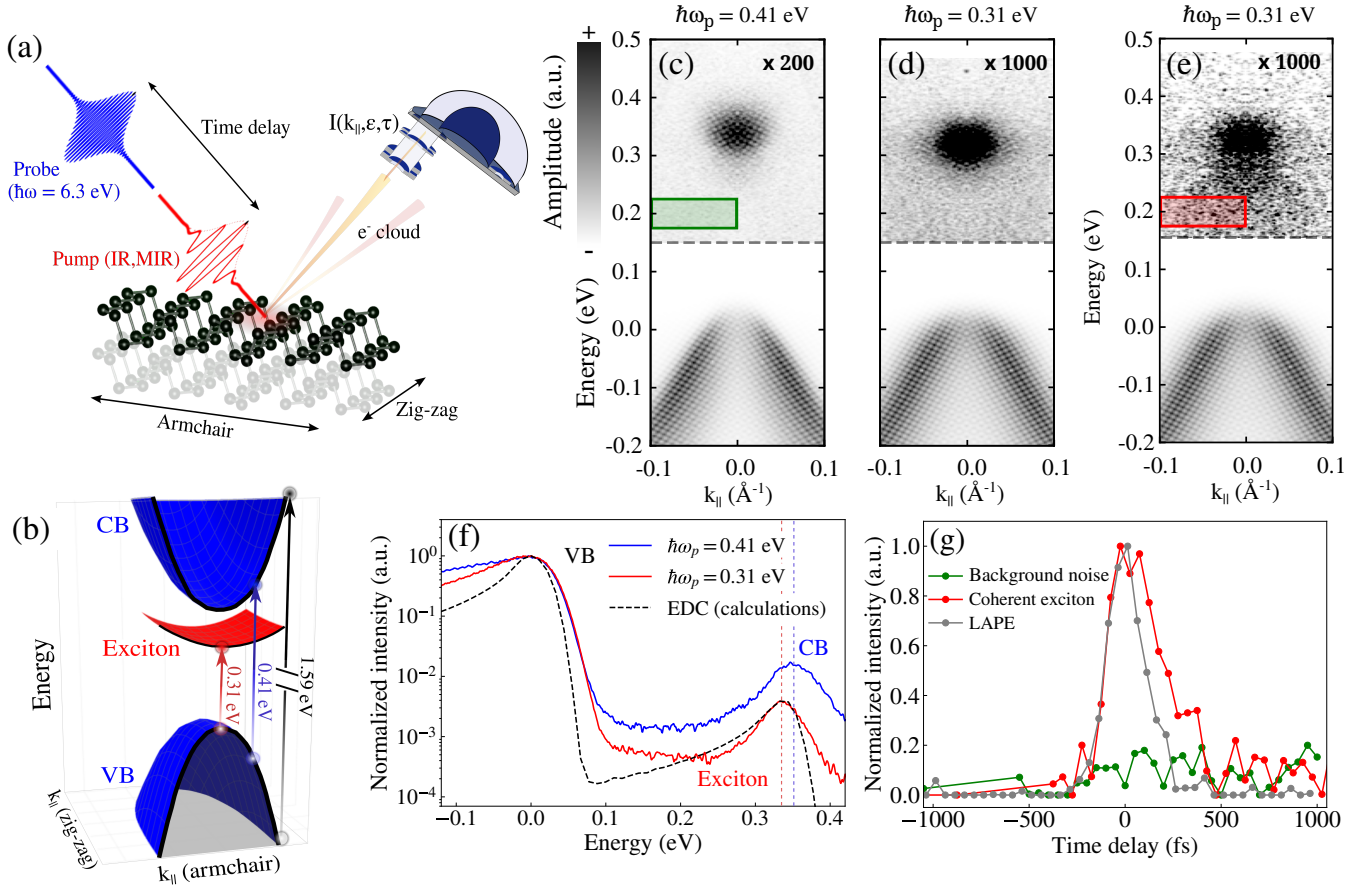


FIG. 1. Observation of excitons in bulk black phosphorus. (a) Sketch of the experimental setup. Electrons are excited by either a IR or MIR pulse and photoemitted by a $\hbar\omega_{pr} = 6.3$ eV pulse. (b) Dispersion of the valence band (VB), conduction band (CB), and the exciton state in the band gap. The arrows show the different excitation energies used in the experiments: $\hbar\omega_p = 1.55$ eV (black), $\hbar\omega_p = 0.41$ eV (blue) and $\hbar\omega_p = 0.31$ eV (red). The latter photon energy is resonant with the coherent exciton at $\mathbf{Q} = 0$. (c) Pump-probe ARPES spectrum acquired with pump photon energy $\hbar\omega_p = 0.41$ eV along the armchair direction, integrated from 500 fs to 10 ps. The data are symmetrized around $k_{\parallel} = 0$ \AA^{-1} . (d) Pump-probe ARPES spectrum as in (c), but with pump photon energy $\hbar\omega_p = 0.31$ eV. A downwards energy shift of the dominant feature in the unoccupied states is observed compared to (c). (e) Pump-probe ARPES spectrum as in (d), but integrated from -200 fs to +200 fs, showing a transient signal inside the band gap. (f) Energy distribution curves (EDC) extracted from panels (c) and (d) in the momentum range $[-0.05, 0.05]$ \AA^{-1} , together with the calculated EDC (see main text). The black, red and blue dashed lines indicate the energy position of the VB maximum, exciton peak and CB, resp.. (g) Transient photoemission intensity extracted from the region of interest (ROI) indicated in panel (e) for the $\hbar\omega_p = 0.31$ eV pump, corresponding to the coherent exciton (with *s*-polarized pump light) and the laser-assisted photoemission (LAPE) (with *p*-polarized pump light). Both curves are normalized to their maximum intensity. The green curve, the intensity of which is scaled for visibility, represents the background signal from the ROI indicated in panel (c) for the $\hbar\omega_p = 0.41$ eV pump.

directly observe the formation of coherent excitons at zero center-of-mass momentum, and track their redistribution in energy-momentum space on a few-picosecond timescale. A key feature of our work is the modeling philosophy: rather than computing the exciton-phonon coupling from first principles, we develop a comprehensive simulation of the trARPES response that incorporates the full complexity of photoemission – photoemission matrix elements, out-of-plane momentum (k_z) broadening, laser pulse parameters, the *ab initio* exciton dispersion, and the real-time quantum kinetics of exciton populations and coherences. This level of quantitative modeling, which we believe has not previously been achieved for

exciton dynamics measured by trARPES, enables us to use the experimental data not just as a benchmark but as a precise constraint on the underlying microscopic parameters. By optimizing the agreement between simulation and experiment across multiple energy-momentum regions simultaneously, we extract the exciton-phonon coupling strength and determine the coherence lifetime with quantitative reliability.

Our results reveal that intravalley exciton-phonon scattering suppresses the coherence of the bright exciton within a few tens of femtoseconds, converting it into a long-lived population of dark, finite-momentum excitons that persists for tens of picoseconds. This scattering is driven by phonon absorp-

tion rather than emission. Comparison with measurements at higher pump photon energies reveals markedly different relaxation pathways and timescales, underscoring the sensitivity of the nonequilibrium dynamics to the initial excitation. Our findings establishes BP as a model system for disentangling coherent and incoherent exciton dynamics and highlights intravalley scattering as a fundamental limitation for coherent exciton phenomena in single-valley semiconductors.

RESULTS

Observation of resonantly populated excitons

We perform trARPES in the pump-probe scheme to photoexcite excitons in BP and follow their ultrafast dynamics. In our experiment, we use variable pump photon energies and a probe photon energy of 6.3 eV [see Fig. 1(a)]. Note that BP is highly anisotropic with a rectangular surface Brillouin zone [34]. We focused on the most dispersive direction and show in Fig. 1 trARPES data obtained along the armchair direction near the Γ point. In graph Fig. 1(c), the data are averaged for time delays between 500 fs and 10 ps for a photoexcitation energy of 0.41 eV, which is larger than the band gap of BP [see Fig. 1(b)]. At this photon energy and in this time delay range, the very bottom of the lowest conduction band (CB) is directly populated by electrons excited from the top of the valence band (VB). Both bands, demarcating a band gap of about 0.3 eV, are observed in Fig. 1(c), in which the energy is referenced with respect to the maximum of the VB. We then reduce the excitation energy to 0.31 eV, comparable with the band gap size. In the corresponding trARPES data of Fig. 1(d), the intensity near the position of the CB adopts a slightly different distribution in energy and momentum space. To make it more obvious, we plot in Fig. 1(f) the energy distribution curves (EDC) integrated over a momentum range near the band extrema ($[-0.05, 0.05] \text{ \AA}^{-1}$) for the two different photoexcitation photon energies. While the position of the leading edge of the VB matches well in both cases, we see that the peak above the VB is shifted to lower energies by 14 meV for the 0.31 eV photoexcitation (red curve), compared to the position of the CB (grey curve) for the 0.41 eV photoexcitation. This energy shift is similar to the expected exciton binding energy E_{ex} in bulk BP [35]. This is the first evidence that we are able to resonantly photoexcite excitons in bulk BP.

We then turn to the transient evolution of the photoemission intensity. For this purpose, ARPES data integrated from -200 fs to +200 fs are displayed in Fig. 1(e). Interestingly, some signal appears in the band gap of BP, showing a downward dispersion *below* the CB. This is reminiscent of the dispersion expected for excitons in semiconductors at early times [19, 36]. We then plot in Fig. 1(g) the photoemission signal *inside* the band gap, at about 0.2 eV above the VB maximum (VBM). While the transient signal acquired with above-band-gap photoexcitation (0.41 eV, green curve) is mainly noise with slow dynamics coming from the tail of the VB, we see a drastically different behavior in the case of near-band-gap photoexcita-

tion (0.31 eV, red curve). An asymmetric peak appears near t_0 . This in-gap signal, featuring a short, but non-zero lifetime, is our second evidence of a transient excitonic signal. Up to now, *s*-polarized photons were used for photoexcitation. Note that we have carefully optimized our probe-laser polarization waveplate angle by minimizing the laser-assisted photoemission (LAPE) signal on the reference material Bi_2Se_3 (see SM). We overlay on the same graph the cross-correlation signal (gray curve) obtained by rotating the photoexcitation polarization to *p*, for which the LAPE signal is dominating. This highlights the excitonic contribution that persists at times later than 500 fs.

Having established our capability to resonantly photoexcite excitons in bulk BP, we now inspect their ultrafast dynamics in more detail. In Fig. 2 we present the transient ARPES intensity extracted from different regions of interest (ROI) at different energies above the VB [see Fig. 2(a) for their positions]. The three curves displayed in graphs 2(b) to 2(d) show a distinct evolution as their respective energy increases towards the CB minimum *from below*. The asymmetric peak at t_0 vanishes, giving way to a rounded step function with a delayed maximum. We attribute the peak at t_0 to the resonant formation of bright excitons with center-of-mass momentum $\mathbf{Q} = 0$. These bright excitons scatter with phonons into dark $\mathbf{Q} \neq 0$ excitons that appear at energies closer to the CB minimum (CBM) in our experimental data after a short time delay.

Quantum-kinetic theoretical framework

To gain microscopic insight into the exciton dynamics observed in our experiments, we performed simulations of the exciton dynamics in BP based on a quantum-kinetic treatment. As the first ingredient, we calculated the exciton states in bulk BP by solving the Bethe-Salpeter equation (BSE) on top of a GW quasiparticle band structure [37]. Here, we employed the method from ref. [38], combining a Wannier tight-binding model [39] for the quasiparticle bands with effective Coulomb interactions determined from the constrained random phase approximation (cRPA) [40]. This approach, which is similar to those presented in refs. [41, 42], allows us to use the very dense momentum grids necessary to accurately capture the small exciton binding energies. The resulting exciton band structure is shown in Fig. 3(a), revealing a binding energy of about 20 meV for the lowest-energy exciton at $\mathbf{Q} = 0$. This value is consistent with the upper bound of 30 meV established in ref. [27]. The exciton dispersion exhibits a pronounced anisotropy between the armchair and zigzag directions, reflecting the underlying electronic band structure of BP.

Solving the BSE also yields the exciton envelope functions $\Lambda^{\lambda, \mathbf{Q}}(\mathbf{k})$ [43], which define the many-body wave function of an exciton in a state λ with center-of-mass momentum \mathbf{Q} by

$$|\Psi^{\lambda, \mathbf{Q}}\rangle = \sum_{\mathbf{k}} \Lambda^{\lambda, \mathbf{Q}}(\mathbf{k}) \hat{c}_{\mathbf{k}+\mathbf{Q}}^\dagger \hat{d}_{\mathbf{k}} |\Psi_0\rangle. \quad (1)$$

Here, $\hat{c}_{\mathbf{k}}^\dagger$ ($\hat{d}_{\mathbf{k}}$) creates (annihilates) an electron in the conduction (valence) band with momentum \mathbf{k} , and $|\Psi_0\rangle$ is the electronic ground state.

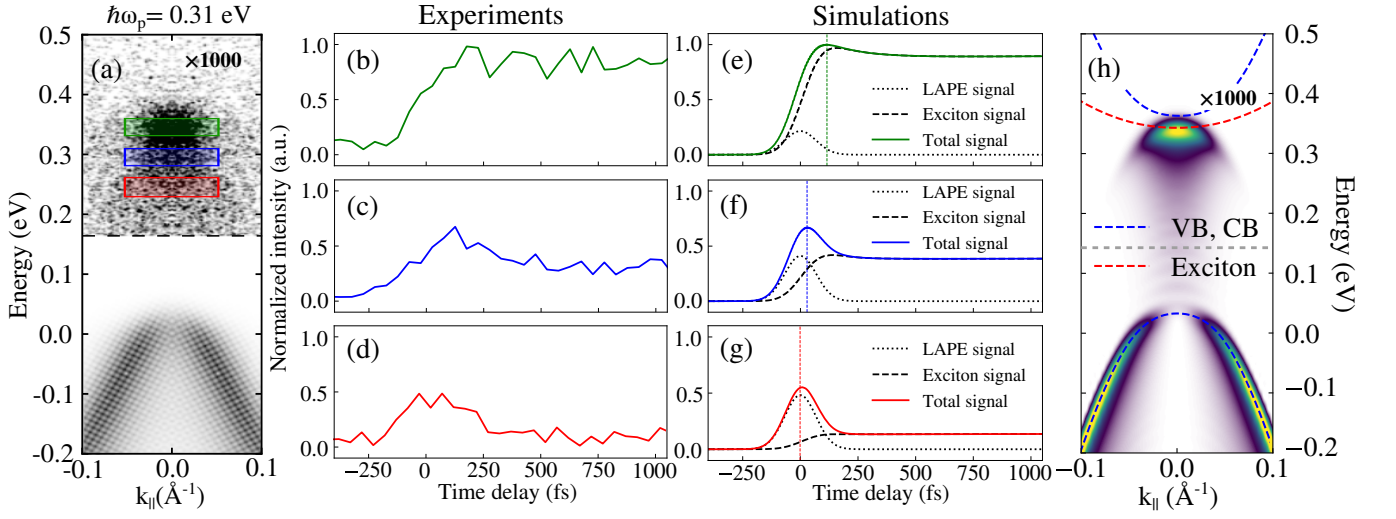


FIG. 2. **Transient dynamics of excitons.** (a) ARPES spectrum acquired with near-band-gap photoexcitation (0.31 eV) for overlapping pump and probe pulses. The colored boxes indicate the regions of interest (ROI) at which the transient dynamics are extracted in panels (b)-(g). (b)-(d) Transient photoemission intensity in different ROI, as indicated in panel (a). The curves are normalized to the maximum value of the ROI with the highest intensity. (e)-(g) Corresponding simulated transient photoemission intensity in the same ROI indicated in panel (a), including both exciton and LAPE contributions. (h) Simulated trARPES intensity for overlapping pump and probe pulses. The dashed lines mark the dispersion of the VB and CB, as well as the exciton dispersion. The ROI for the simulated spectrum are equivalent to the ones in panel (a). The spectra in panel (a) has been scaled by a factor of 1000 above the gray dashed line as well as the exciton's signal in panel (h).

With the exciton states at hand, we turn to the ultrafast exciton dynamics. Describing the time evolution of excitons in the presence of a laser excitation and exciton-phonon interactions is a challenging many-body problem [44]. Here we employ a quantum-kinetic approach inspired by the semiconductor Bloch equations [10, 45] combined with the time-dependent Boltzmann equation [46, 47]. In this framework, we describe the exciton dynamics in terms of the exciton density matrix $\rho_{\alpha\beta}(t)$, where $\alpha, \beta \in \{0, \mathbf{Q}\}$ label the ground state (0) and exciton states with momentum \mathbf{Q} . The diagonal elements with $\alpha = \mathbf{Q}$ correspond to the population $N_{\mathbf{Q}}(t)$ of excitons with momentum \mathbf{Q} , while the off-diagonal elements describe coherences between different exciton momentum states. In particular, the coherences $\rho_{0\mathbf{Q}}(t)$ directly describe the coherent exciton polarization induced by the laser field. The time evolution of the density matrix is governed by the equation of motion

$$\frac{d}{dt}\rho(t) = -i[\mathbf{H}^{\text{exc}}(t), \rho(t)] + \mathbf{S}(t). \quad (2)$$

The excitonic Hamiltonian $H_{\alpha\beta}^{\text{exc}}(t) = E_{\alpha}\delta_{\alpha\beta} - \mathbf{E}(t) \cdot \mathbf{D}_{\alpha\beta}$ contains the ground-state energy $E_{\alpha} = E_0$ (exciton energies $E_{\alpha} = E_x(\mathbf{Q})$) and the coupling to the time-dependent electric field $\mathbf{E}(t)$ via the excitonic dipole matrix elements $\mathbf{D}_{\alpha\beta}$. The electric field is modeled as a Gaussian laser pulse with the same pulse duration as the time cross-correlation in the experiments; the peak electric field $E^{(0)}$ is kept as a free parameter to match the experimental excitation density.

The diagonal part $S_{\alpha\alpha}(t)$ of the scattering term describes exciton-phonon scattering processes, which we include at the

level of the quantum master equation

$$S_{\mathbf{Q}\mathbf{Q}}(t) = \frac{2\pi\gamma^2}{N_{\mathbf{Q}}} \sum_{\mathbf{Q}'} [\Gamma_{\mathbf{Q}'\rightarrow\mathbf{Q}}N_{\mathbf{Q}'}(t) - \Gamma_{\mathbf{Q}\rightarrow\mathbf{Q}'}N_{\mathbf{Q}}(t)]. \quad (3)$$

The scattering rates $\Gamma_{\mathbf{Q}\rightarrow\mathbf{Q}'}$ are defined in terms of the acoustic phonon modes of BP and the exciton-phonon coupling matrix elements. We characterize them by the mode-averaged coupling strength γ , which is the only free parameter in our model besides $E^{(0)}$. The off-diagonal part is treated within the relaxation-time approximation $S_{\alpha\beta} = [S_{\alpha\alpha} + S_{\beta\beta}]/2$, which has been shown to accurately capture dephasing processes [46, 47]. Our approach is similar to the excitonic Bloch equations from ref. [12] in the low-density regime, except for one key difference: the exciton-phonon coupling γ corresponds to the unscreened coupling strength.

The quantum kinetic equation of motion (2), using the experimentally relevant laser pulse parameters, provides a microscopic description of the exciton dynamics in BP, capturing the coherent exciton generation and incoherent relaxation on the same footing. To directly compare with the experimental trARPES data, we compute the time-resolved photoemission intensity following refs. [36, 38, 48, 49]:

$$I(\mathbf{k}_{\parallel}, \omega, \tau) = \sum_{\mathbf{Q}} N_{\mathbf{Q}}(\tau) \int dk_z F(k_z - p_{\perp}) |M_c(\mathbf{k}, p_{\perp})|^2 \times |\Lambda^{\lambda, \mathbf{Q}}(\mathbf{k}, k_z)|^2 \delta(\epsilon_v(\mathbf{k} - \mathbf{Q}) + E_x(\mathbf{Q}) + \omega_{\text{pr}} - \omega) + I_{\text{LAPE}}(\mathbf{k}_{\parallel}, \omega, \tau). \quad (4)$$

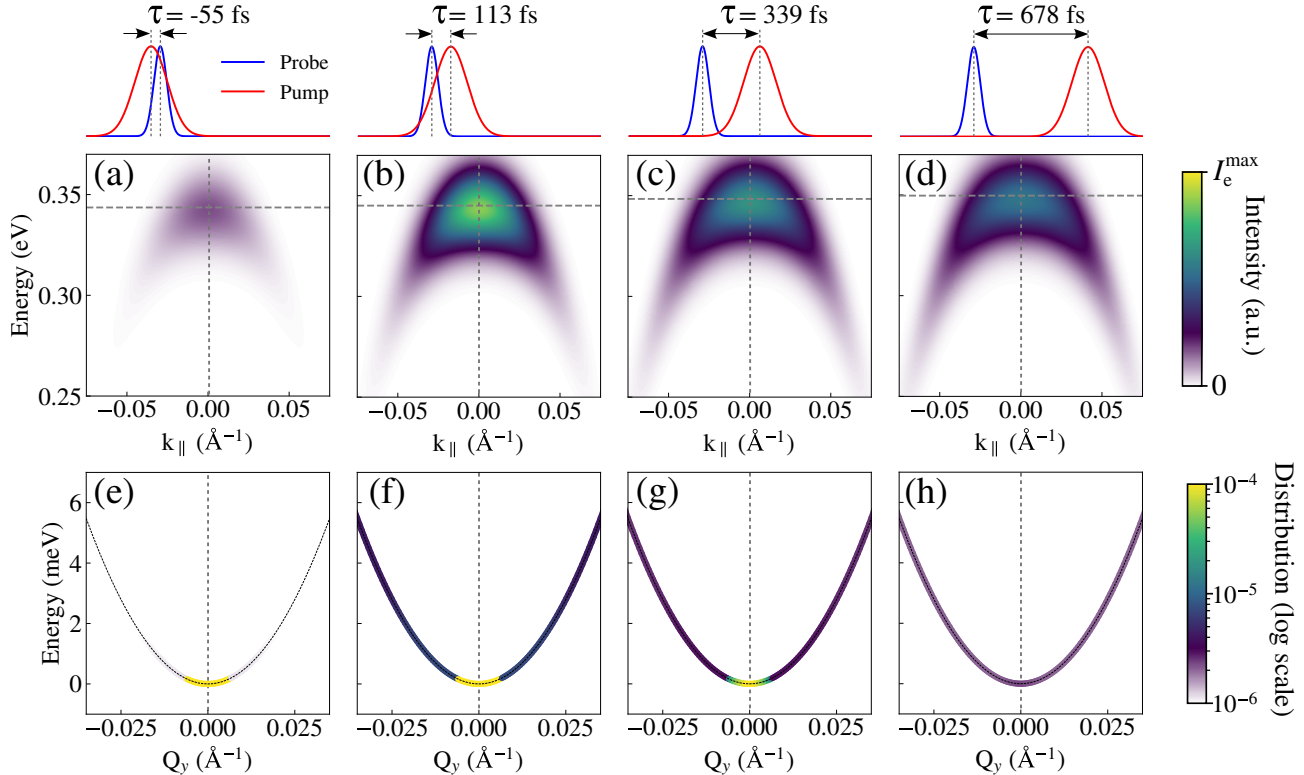


FIG. 3. **Exciton scattering dynamics.** (a)-(d) Simulated trARPES intensity for different time delays (as sketched above). The gray dashed lines indicate the center of mass of momentum and energy at each time delay. (e)-(h) Exciton distribution $N_{\mathbf{Q}}(t)$ for time delays τ as in (a)-(d). The black dashed lines show the exciton dispersion.

Here, \mathbf{k}_{\parallel} and ω are the in-plane momentum and energy of the emitted photoelectrons, τ is the pump-probe delay, and ω_{pr} is the probe photon energy. Going beyond the usual treatment of 2D systems, we also include the out-of-plane momentum p_{\perp} of the photoelectrons (determined by energy conservation) and account for the finite mean-free path by the Lorentzian function $F(k_z - p_{\perp})$. Note that we have specialized to the case of a single exciton band λ and single valence/conduction band for clarity. To account for the pronounced polarization dependence of the ARPES signal, we include the photoemission matrix element of the conduction band $M_c(\mathbf{k}, p_{\perp})$, which we compute as in ref. [50]. As the first step we fixed the peak field strength $E^{(0)}$ by computing the time-integrated EDC and matching the intensity of the exciton peak to the experimental data [Fig. 1(f)]. This yields an excitation density of about $n_e \simeq 2 \times 10^{16} \text{ cm}^{-3}$, which corresponds to the low-density limit for 3D semiconductors with well-defined excitons [51]. Before we can compare the time-resolved photoemission intensity, Eq. (4), to the experimental data, we need to account for LAPE effects. While the experimental geometry has been calibrated to minimize LAPE contributions for s -polarized pump pulses, a residual LAPE signal is still observed in the experiments. This is potentially due to imperfect polarization control in the

experimental setup, leading to a small p -polarized component in the pump beam. Another possibility is the non-trivial interaction of the pump field with the sample surface – which has been discussed as Coulomb-laser coupling in the context of attosecond photoemission from atoms, which can induce LAPE even with nominal s -polarization. This effect is probably more important in our case due to the low photon energy of the probe. In trARPES, the LAPE contribution appears as a replica of the VB shifted by the pump photon energy; its intensity scales with the pump-probe time overlap and decays on the timescale of the pump pulse duration. This is accounted for by the term $I_{\text{LAPE}}(\mathbf{k}_{\parallel}, \omega, \tau)$ in Eq. (4) (see Supplemental Materials for more details).

Ultrafast dynamics of excitons

With these ingredients, we can directly compare the simulated trARPES intensity to the experimental data of Fig. 2. In the calculated spectrum at t_0 [Fig. 2(h)], we can clearly identify the exciton peak below the CB, as well as the faint spectral features dispersing downward. This is the signature expected for coherent excitons ($N_{\mathbf{Q}} = 0$ for $\mathbf{Q} \neq 0$) [36], as the energy conservation condition in Eq. (4) corresponds to the VB dispersion shifted by the exciton energy $E_x(\mathbf{Q} = 0)$. Similar features are present in the experimental data, confirming the

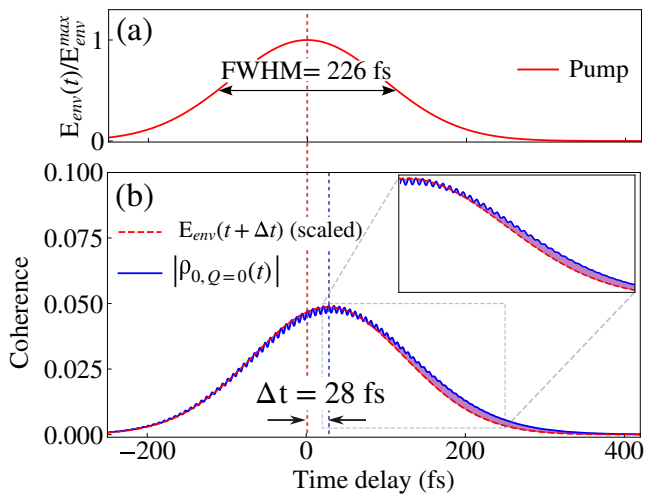


FIG. 4. **Exciton coherence.** (a) Envelope of the IR pump pulse and its corresponding FWHM of 226 fs, normalized to its maximum. (b) Absolute value of the coherence between the ground state and the coherent exciton, $\rho_{0,\mathbf{Q}=0}(t)$. Together with it, we plot the envelope of the electric field scaled to the maximum of the absolute value of the coherence and shifted by Δt (time difference between the maximum of the coherence and the pump pulse). Thus, we highlight the shift between them and the asymmetric behavior of the coherence in comparison with the field.

excitonic nature of the observed in-gap signal. Now we revisit the transient dynamics in the three distinct ROI indicated by the colored boxes in Fig. 2(a): (i) the ROI with maximum exciton intensity (green box), (ii) an intermediate ROI capturing the coherent exciton signal (blue box), and (iii) a ROI in the gap (red box). The corresponding transient dynamics extracted from the experimental and simulated trARPES data are shown in Fig. 2(b)-(g). Achieving agreement between experiment and theory across all ROI is only possible by a unique choice of the effective exciton-phonon coupling strength ($\gamma \simeq 2.5 \times 10^{-4}$ a.u.) and LAPE intensity. First-principles derivations of the Excitonic Bloch Equations (EBEs) have shown that standard model Hamiltonians are often overscreened in the electron-phonon couplings (due to a double-counting of the dielectric response). However, by fitting γ directly to the experimental trARPES dynamics and staying in the low density regime, our effective γ corresponds to the irreducible coupling case, capturing the physical scattering rates [12, 48]. The lowest energy ROI in Fig. 2(d),(g) shows a pronounced peak close to delay $\tau = 0$ that quickly decays. Nevertheless, a slightly asymmetric tail is visible. The theory indicates that this part of the signal is due to LAPE, with a small exciton contribution responsible for the asymmetry. Moving to the intermediate ROI [see Fig. 2(c),(f)], the exciton contribution becomes more prominent, leading to a clear asymmetric peak with a delayed maximum and persistent intensity on the picosecond time scale. Finally, in the ROI with maximum exciton intensity [Fig. 2(b),(e)], the LAPE contribution is negligible, and the transient dynamics is fully dominated by the exciton popu-

lation. Here, we observe a pronounced delayed rise of the signal, reflecting the phonon-assisted scattering of excitons from $\mathbf{Q} = 0$ to nonzero momentum states. Overall, we find excellent agreement between experiment and theory for all three ROI, confirming our microscopic understanding of the ultrafast exciton dynamics in BP.

The different time delays of the maximum intensity in the three ROI can be understood by the transition from a coherent exciton population at $\mathbf{Q} = 0$ to an incoherent population at $\mathbf{Q} \neq 0$. Using the predictive power of our quantum-kinetic model, we can directly track the time evolution of the exciton populations $N_{\mathbf{Q}}(t)$ and coherences $\rho_{0\mathbf{Q}}(t)$. In Fig. 3(a)-(d), we show the simulated trARPES intensity at different time delays and in Fig. 3(e)-(h) the corresponding exciton populations. As time progresses, the initially coherent exciton population at $\mathbf{Q} = 0$ (bright excitons) rapidly scatters with acoustic phonons, redistributing the exciton population to nonzero momentum states (dark excitons). In the trARPES intensity, this leads to a shift of the maximum intensity towards the CBM, indicated by the gray horizontal lines in Fig. 3(a)-(d).

In our theory we have direct access to the coherence dynamics $\rho_{0,\mathbf{Q}=0}(t)$ (corresponding to a macroscopic time-dependent polarization), which is not directly measurable in our experiments. The coherence closely follows the shape of the laser pulse [Fig. 4(a),(b)], indicating that the coherent exciton population is predominantly present during the pump pulse duration and decays rapidly afterwards (indicated by the asymmetric shape). The delay between the peak of the coherence and the pump $\Delta t \sim 28$ fs is related to both population and decoherence dynamics. With the exciton-phonon coupling strength γ determined above, we obtain a coherence lifetime from the tail asymmetry, obtaining $T_{\text{coh}} \simeq 40$ fs.

To systematically explore excitation regimes that are off-resonant with respect to the exciton, we performed further trARPES measurements with a pump photon energy of $\hbar\omega_p = 1.59$ eV. Within this regime, multiple studies on the non-equilibrium dynamics have been conducted. Previous trARPES works revealed that photoexcited BP hosts a variety of non-equilibrium effects, including surface photovoltage [52], transient Stark broadening and band gap renormalization at high excitation densities [53–55]. Here, we want to focus on the population dynamics at $\hbar\omega_p = 1.59$ eV in comparison to data taken at smaller pump photon energies discussed in relation to Fig. 1. The trARPES spectrum in Fig. 5(a) reveals that under this photon excitation energy, electrons are injected in states far above the CBM, partially exceeding the detector window. To highlight the intraband dynamics, we choose ROI in ascending energy and trace the respective signal intensity as a function of delay time. In Fig. 5(c), we resolve a clear cascade of excited carriers from the highest ROI in energy to the CBM. Remarkably, the relaxation dynamics proceed on an unexpectedly slow timescale: the signal in the highest energy ROI (yellow box) only reaches its maximum 750 fs after excitation, and the population at the CBM peaks after nearly 2 ps. In contrast, the excitation with photon energy just above the

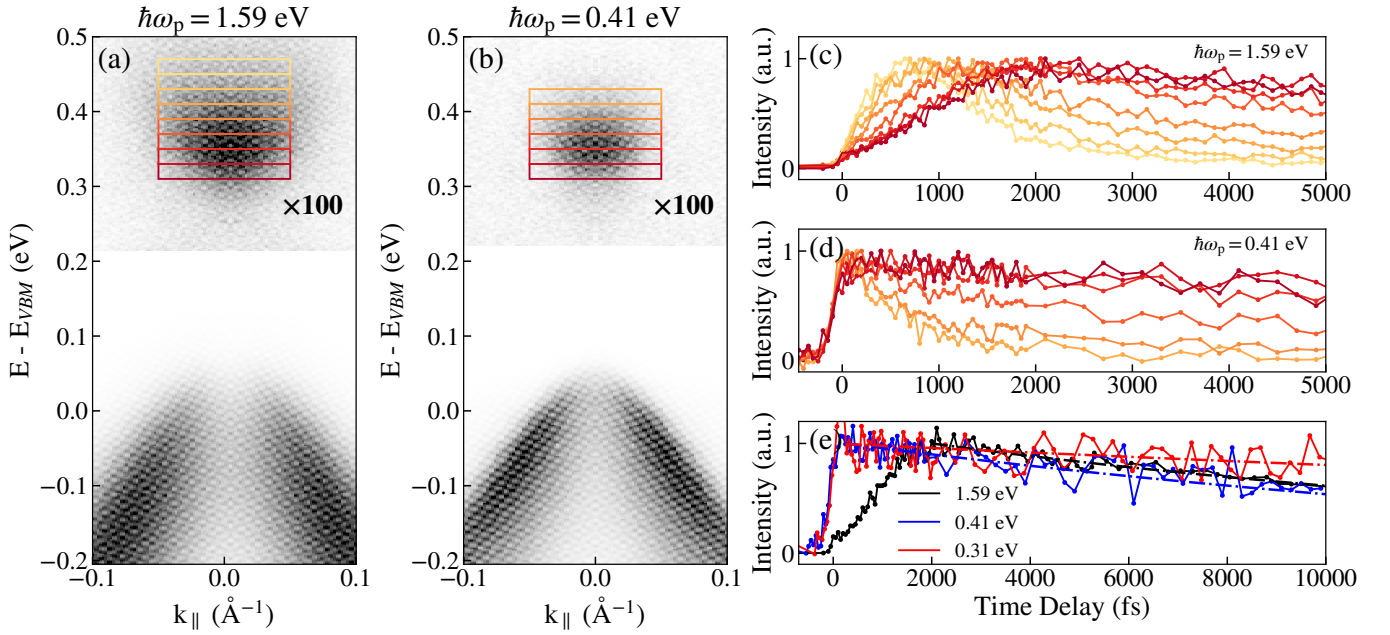


FIG. 5. **Comparison of the Dynamics in different Pump Regimes.** (a) Pump-probe ARPES spectra acquired with a pump photon energy of $\hbar\omega_p = 1.55$ eV integrated from t_0 to $+1$ ps. (b) Pump-probe ARPES spectra acquired with a pump photon energy of $\hbar\omega_p = 0.41$ eV, integrated from t_0 to $+1$ ps. (c) Normalized time traces extracted in the ROI highlighted in (a). (d) Normalized time traces extracted in the ROI highlighted in (b). (e) Comparison of the long-time relaxation of the signal at the CBM in the lowest energy ROI in (a) and (b). The red curve was extracted at the corresponding energy-momentum ROI in the spectrum with a pump photon energy of $\hbar\omega_p = 0.31$ eV, shown in Fig. 1(d). To quantify the interband relaxation, a fit with a single exponential decay function was performed to reveal respective carrier lifetimes of $\tau = 16.5$ ps (1.59 eV), 20.6 ps (0.41 eV), and 56.4 ps (0.31 eV). All curves are normalized w.r.t the starting value of the fit.

band gap ($\hbar\omega_p = 0.41$ eV) directly populates the CBM at $\bar{\Gamma}$. Consequently, only the low-energy region of the CB is occupied, as shown in Fig. 5(b). The direct excitation into the CB also manifests in the intraband relaxation in Fig. 5(d). The regions of higher energy reach their maximum signal almost immediately after the initial excitation and even in the lowest energy region, the signal peaks after 100 fs only, highlighting the much faster dynamics. This difference in the time scales suggests that the relaxation pathway strongly depends on the energy of the photoexcited carriers. At high pump photon energies, higher energy states in the CB can be directly populated. The transition from these high-energy states to lower energy states in the CB is emerging as a potential bottleneck for relaxation [32].

Charge carrier dynamics above the band gap

To study the recombination of photoexcited electrons and holes, in Fig. 5(e) we compare the dynamics of carriers at the bottom of the CB for the three different excitation regimes, corresponding to the formation of excitons (red), the direct occupation of the CB (blue), and the indirect filling of the CB (black). To isolate the recombination dynamics from intraband relaxation mechanisms, only the signals in the lowest energy ROI (dark red box in Fig. 5(a) and Fig. 5(b) and the corresponding position in Fig. 1(d)) are shown. Despite the pronounced difference in the rise time, the curves show a similar decay of free carriers in the CB, regardless of whether they

were excited with the 1.59 eV or the 0.41 eV pulses. Exponential fits support this, yielding relaxation times of 16.5 ps and 20.6 ps and indicating that the recombination dynamics are nearly independent of the initial excitation and relaxation pathway. For the case of a photoexcitation resonant with excitonic states (0.31 eV), the relaxation time is much longer, namely 56.4 ps. This is consistent with the fact that for excitons, being bound electron-hole pairs, additional energy must be provided to break the pairs before recombination can take place, enhancing their relaxation time in comparison to free charge carriers. This also indicates that a negligible amount of free carriers are excited at this pump photon energy.

DISCUSSION AND CONCLUSION

In this study, we generated coherent excitons with zero center-of-mass momentum by direct photoexcitation with a photon energy similar to the band gap of BP. Experimentally, evidence for the creation of such excitons comes from the energy position of the excitonic peak in comparison to free carriers excited in the CB with off-resonant photoexcitation. Additionally, we followed their transient dynamics over a few picoseconds and observed that the in-gap signal due to the excitonic contribution displays a distinct energy dependence. Moreover, by carefully extracting the relaxation time of free charge carriers excited at higher energies, we singled out the

relaxation time of the excitons that extends to longer delay times.

A quantum-kinetic calculation based on the Bethe-Salpeter equation and extended to the semiconductor Bloch equation combined with the time-dependent Boltzmann equation including coupling to acoustic phonons allowed us to interpret the experimental data with high fidelity. In about 30 fs, scattering with phonon leads to the full decoherence of the excitons which are scattered into dark excitons carrying non-zero center-of-mass momentum. From the comparison to experimental curves, we extracted a quantitative value for the exciton-phonon coupling strength, which sets a benchmark for state-of-the-art *ab initio* methods for calculating exciton-phonon coupling and exciton linewidth [8, 13, 56]. The scattering process redistributing the excitons in their intrinsic dispersion is driven by phonon absorption. This is at odds with other recent experiments probing excitons that are generated indirectly by a non-resonant process, after which excited charge carriers relax towards the band extrema [57, 58]. In these experiments, the excited free carriers, and eventually the excitons, emit phonons, leading to the warming of the lattice.

Our work reveals that exciton scattering with acoustic phonons is highly efficient in three-dimensional bulk BP, leading to a rapid loss of excitonic coherence on ultrashort timescales. Importantly, we identify intravalley phonon scattering as the sole decoherence mechanism in this system, in stark contrast to transition-metal dichalcogenides, where intervalley scattering into momentum-forbidden states is widely recognized as the dominant relaxation pathway [21, 59, 60]. This result demonstrates that excitonic coherence can be fundamentally limited by intravalley processes alone, even in the absence of a multivalley band structure. As a consequence, our findings place stringent constraints on the possibility of coherently manipulating excitons — and thereby the electronic structure of bulk BP — using optical excitation beyond the initial ultrafast regime. Extending the combined experimental and theoretical approach presented here to few-layer BP, where reduced dimensionality and modified phonon spectra may alter the exciton-phonon coupling, represents an exciting direction for future investigations.

MATERIALS AND METHODS

Sample growth

Large single crystals of BP were synthesized by a modified chemical vapor transport technique as reported in Ref. [61]. Red phosphorus (400 mg, > 99.7%, powder), SnI₄ (8 mg, 99%), and Sn (16 mg, 99.995%, powder) were sealed in an evacuated quartz ampoule. The ampoule was placed horizontally in a muffle furnace and partially covered on one side with ceramic elements in order to establish a controlled temperature gradient along the ampoule. The furnace was heated to 650°C at a rate of 600°C per hour, followed by a multi-step cooling program consisting of cooling to 550°C over 1 h, to 500°C

over 8 h, and subsequently to 200°C over 2 h, followed by rapid cooling by switching off the furnace. Manually selected crystals were sealed in an evacuated quartz ampoule and placed in a tubular furnace with one end of the ampoule extending outside the heated zone. The sample was heated to 200°C for 3 h in order to remove residual SnI₄ and elemental iodine. The obtained crystals were then rinsed sequentially with acetone (Ac), water, and analytical ethanol (EtOH), followed by drying under dynamic vacuum.

Time-resolved ARPES

trARPES experiments were carried out using a Scienta DA30 hemispherical photoelectron analyzer with a base pressure better than 5×10^{-11} mbar. For the light source, half of the power of a femtosecond laser (Pharos, Light Conversion, operating at 1030 nm) is converted into 780 nm (1.59 eV) light with an optical parametric amplifier, which is then frequency-quadrupled to 6.3 eV in β -BaB₂O₄ crystals to generate UV pulses (see e.g. ref. [62]), which were later-on *p*-polarized. The intrinsic resolution of the UV pulse is 25 meV, as determined by the fit of the Fermi edge of a polycrystalline metal. The remaining half of the fundamental laser power is directed into a collinear optical parametric amplifier (Orpheus, Light Conversion) to generate IR pulses at 1.55, 0.41 or 0.31 eV. The total temporal resolution was determined to be better than 100 fs, 160 fs and 240 fs, respectively, by measuring the width of the photoemission cross-correlation between the pump and the probe pulses. The pump-probe measurements were performed at 200 kHz and the incident fluence used to detect the exciton was of the order of $F \approx 46 \mu\text{J}/\text{cm}^2$. Unless specified otherwise, the pump laser was *s*-polarized.

The slit of our hemispherical analyzer is oriented such that the parallel momentum is running along the armchair direction. All data have been acquired at the temperature of $T_0 = 80$ K.

-
- [1] G. Wang, A. Chernikov, M. M. Glazov, T. F. Heinz, X. Marie, T. Amand, and B. Urbaszek, *Colloquium* : Excitons in atomically thin transition metal dichalcogenides, *Rev. Mod. Phys.* **90**, 021001 (2018).
 - [2] F. Gucci, E. B. Molinero, M. Russo, P. San-Jose, F. V. A. Carmargo, M. Maiuri, M. Ivanov, A. Jiménez-Galán, R. E. F. Silva, S. Dal Conte, and G. Cerullo, Encoding and manipulating ultrafast coherent valleytronic information with lightwaves, *Nat. Photon.* **20**, 266 (2026).
 - [3] J. Kasprzak, M. Richard, S. Kundermann, A. Baas, P. Jeambrun, J. M. J. Keeling, F. M. Marchetti, M. H. Szymańska, R. André, J. L. Staehli, V. Savona, P. B. Littlewood, B. Deveaud, and L. S. Dang, Bose-Einstein condensation of exciton polaritons, *Nature* **443**, 409 (2006).
 - [4] Y. Kobayashi, C. Heide, A. C. Johnson, V. Tiwari, F. Liu, D. A. Reis, T. F. Heinz, and S. Ghimire, Floquet engineering

- of strongly driven excitons in monolayer tungsten disulfide, *Nature Physics* **19**, 171 (2023).
- [5] V. Pareek, D. R. Bacon, X. Zhu, Y.-H. Chan, F. Bussolotti, M. G. Menezes, N. S. Chan, J. P. Urquizo, K. Watanabe, T. Taniguchi, E. Perfetto, M. K. L. Man, J. Madéo, G. Stefanucci, D. Y. Qiu, K. E. J. Goh, F. H. da Jornada, and K. M. Dani, Driving Floquet physics with excitonic fields, *Nature Physics* **22**, 209 (2026).
- [6] Y.-H. Chan, D. Y. Qiu, F. H. da Jornada, and S. G. Louie, Giant self-driven exciton-Floquet signatures in time-resolved photoemission spectroscopy of MoS₂ from time-dependent GW approach, *Proceedings of the National Academy of Sciences* **120**, e2301957120 (2023).
- [7] G. Antonius and S. G. Louie, Theory of exciton-phonon coupling, *Phys. Rev. B* **105**, 085111 (2022).
- [8] Y.-h. Chan, J. B. Haber, M. H. Naik, J. B. Neaton, D. Y. Qiu, F. H. Da Jornada, and S. G. Louie, Exciton Lifetime and Optical Line Width Profile via Exciton-Phonon Interactions: Theory and First-Principles Calculations for Monolayer MoS₂, *Nano Lett.* **23**, 3971 (2023).
- [9] P. Lechiffart, F. Paleari, D. Sangalli, and C. Attaccalite, First-principles study of luminescence in hexagonal boron nitride single layer: Exciton-phonon coupling and the role of substrate, *Phys. Rev. Materials* **7**, 024006 (2023).
- [10] M. Kira and S. Koch, Many-body correlations and excitonic effects in semiconductor spectroscopy, *Prog. Quantum Electron.* **30**, 155 (2006).
- [11] H.-Y. Chen, D. Sangalli, and M. Bernardi, First-principles ultrafast exciton dynamics and time-domain spectroscopies: Dark-exciton mediated valley depolarization in monolayer WSe₂, *Phys. Rev. Research* **4**, 043203 (2022).
- [12] G. Stefanucci and E. Perfetto, Excitonic Bloch equations from first principles, *SciPost Phys.* **18**, 009 (2025).
- [13] Y.-h. Chan, M. H. Naik, J. B. Haber, J. B. Neaton, S. G. Louie, D. Y. Qiu, and F. H. Da Jornada, Exciton-Phonon Coupling Induces a New Pathway for Ultrafast Intralayer-to-Interlayer Exciton Transition and Interlayer Charge Transfer in WS₂-MoS₂ Heterostructure: A First-Principles Study, *Nano Lett.* **24**, 7972 (2024).
- [14] Y.-h. Chan, J. B. Haber, M. H. Naik, S. G. Louie, J. B. Neaton, F. H. Da Jornada, and D. Y. Qiu, Exciton thermalization dynamics in monolayer MoS₂: A first-principles Boltzmann equation study, *Phys. Rev. B* **111**, 184305 (2025).
- [15] H. Mittenzwey, O. Voigt, and A. Knorr, Excitonic theory of the ultrafast optical response of 2d-quantum-confined semiconductors at elevated densities (2026), arXiv:2512.03198 [cond-mat.mes-hall].
- [16] O. Dogadov, H. Mittenzwey, M. Bertolotti, N. Olsen, T. Deckert, C. Trovatiello, X. Zhu, D. Brida, G. Cerullo, A. Knorr, and S. Dal Conte, Dissecting intervalley coupling mechanisms in monolayer transition metal dichalcogenides, *npj 2D Mater Appl* **10**, 21 (2026).
- [17] F. Boschini, M. Zonno, and A. Damascelli, Time-resolved ARPES studies of quantum materials, *Rev. Mod. Phys.* **96**, 015003 (2024).
- [18] M. K. L. Man, J. Madéo, C. Sahoo, K. Xie, M. Campbell, V. Pareek, A. Karmakar, E. L. Wong, A. Al-Mahboob, N. S. Chan, D. R. Bacon, X. Zhu, M. M. M. Abdelrasoul, X. Li, T. F. Heinz, F. H. da Jornada, T. Cao, and K. M. Dani, Experimental measurement of the intrinsic excitonic wave function, *Science Advances* **7**, eabg0192 (2021).
- [19] S. Dong, M. Puppini, T. Pincelli, S. Beaulieu, C. Christiansen, H. Huebener, C. Nicholson, R. Xian, M. Dendzik, Y. Deng, Y. Windsor, M. Selig, E. Malic, A. Rubio, A. Knorr, M. Wolf, L. Rettig, and R. Ernstorfer, Direct measurement of key exciton properties: Energy, dynamics, and spatial distribution of the wave function, *Natural Sciences* **1**, e10010. (2021).
- [20] M. Reutzler, G. S. M. Jansen, and S. Mathias, Probing excitons with time-resolved momentum microscopy, *Advances in Physics: X* **9**, 2378722 (2024).
- [21] R. Bertoni, C. W. Nicholson, L. Waldecker, H. Hübener, C. Monney, U. De Giovannini, M. Puppini, M. Hoesch, E. Springate, R. T. Chapman, C. Cacho, M. Wolf, A. Rubio, and R. Ernstorfer, Generation and evolution of spin-, valley-, and layer-polarized excited carriers in inversion-symmetric WSe₂, *Phys. Rev. Lett.* **117**, 277201 (2016).
- [22] H.-Y. Chen, D. Sangalli, and M. Bernardi, First-principles ultrafast exciton dynamics and time-domain spectroscopies: Dark-exciton mediated valley depolarization in monolayer WSe₂, *Phys. Rev. Res.* **4**, 043203 (2022).
- [23] S. Helmrich, K. Sampson, D. Huang, M. Selig, K. Hao, K. Tran, A. Achstein, C. Young, A. Knorr, E. Malic, U. Woggon, N. Owschimikow, and X. Li, Phonon-assisted intervalley scattering determines ultrafast exciton dynamics in MoSe₂ bilayers, *Phys. Rev. Lett.* **127**, 157403 (2021).
- [24] D. Schmitt, J. P. Bange, W. Bennecke, A. AlMutairi, G. Meneghini, K. Watanabe, T. Taniguchi, D. Steil, D. R. Luke, R. T. Weitz, S. Steil, G. S. M. Jansen, S. Brem, E. Malic, S. Hofmann, M. Reutzler, and S. Mathias, Formation of moiré interlayer excitons in space and time, *Nature* **608**, 499 (2022).
- [25] D. Christiansen, M. Selig, E. Malic, R. Ernstorfer, and A. Knorr, Theory of exciton dynamics in time-resolved ARPES: Intra- and intervalley scattering in two-dimensional semiconductors, *Phys. Rev. B* **100**, 205401 (2019).
- [26] R. Wallauer, R. Perea-Causin, L. Münster, S. Zajusch, S. Brem, J. Gütde, K. Tanimura, K.-Q. Lin, R. Huber, E. Malic, and U. Höfer, Momentum-resolved observation of exciton formation dynamics in monolayer WS₂, *Nano Letters* **21**, 5867 (2021).
- [27] V. Tran, R. Soklaski, Y. Liang, and L. Yang, Layer-controlled band gap and anisotropic excitons in few-layer black phosphorus, *Phys. Rev. B* **89**, 235319 (2014).
- [28] G. Zhang, A. Chaves, S. Huang, F. Wang, Q. Xing, T. Low, and H. Yan, Determination of layer-dependent exciton binding energies in few-layer black phosphorus, *Sci. Adv.* **4**, eaap9977 (2018).
- [29] X. Wang, A. M. Jones, K. L. Seyler, V. Tran, Y. Jia, H. Zhao, H. Wang, L. Yang, X. Xu, and F. Xia, Highly anisotropic and robust excitons in monolayer black phosphorus, *Nature Nanotech* **10**, 517 (2015).
- [30] D. Zahn, P.-N. Hildebrandt, T. Vasileiadis, Y. W. Windsor, Y. Qi, H. Seiler, and R. Ernstorfer, Anisotropic Nonequilibrium Lattice Dynamics of Black Phosphorus, *Nano Lett.* **20**, 3728 (2020).
- [31] A. Montanaro, F. Giusti, M. Zanfrognini, P. Di Pietro, F. Glerean, G. Jarc, E. M. Rigoni, S. Y. Mathengattil, D. Varsano, M. Rontani, A. Perucchi, E. Molinari, and D. Fausti, Anomalous non-equilibrium response in black phosphorus to sub-gap mid-infrared excitation, *Nat Commun* **13**, 2667 (2022).
- [32] G. Shen, X. Tian, L. Cao, H. Guo, X. Li, Y. Tian, X. Cui, M. Feng, J. Zhao, B. Wang, H. Petek, and S. Tan, Ultrafast energizing the parity-forbidden dark exciton in black phosphorus, *Nature Communications* **16**, 3992 (2025).
- [33] M. Dendzik, A. Marini, S. Beaulieu, S. Dong, T. Pincelli, J. Maklar, R. P. Xian, E. Perfetto, M. Wolf, G. Stefanucci, R. Ernstorfer, and L. Rettig, Ultrafast nonlinear Hall effect in black phosphorus (2026).
- [34] E. Golias, M. Krivenkov, and J. Sánchez-Barriga, Disentangling bulk from surface contributions in the electronic structure of black phosphorus, *Phys. Rev. B* **93**, 075207 (2016).

- [35] E. Carré, L. Sponza, A. Lussion, I. Stenger, E. Gauffrès, A. Loiseau, and J. Barjon, Excitons in bulk black phosphorus evidenced by photoluminescence at low temperature, *2D Materials* **8**, 021001 (2021).
- [36] A. Rustagi and A. F. Kemper, Photoemission signature of excitons, *Phys. Rev. B* **97**, 235310 (2018).
- [37] G. Onida, L. Reining, and A. Rubio, Electronic excitations: density-functional versus many-body Green's-function approaches, *Rev. Mod. Phys.* **74**, 601 (2002).
- [38] S. Beaulieu, S. Dong, V. Christiansson, P. Werner, T. Pincelli, J. D. Ziegler, T. Taniguchi, K. Watanabe, A. Chernikov, M. Wolf, L. Rettig, R. Ernstorfer, and M. Schüler, Berry curvature signatures in chiroptical excitonic transitions, *Science Advances* **10**, eadk3897 (2024).
- [39] G. Pizzi, V. Vitale, R. Arita, S. Blügel, F. Freimuth, G. Géranton, M. Gibertini, D. Gresch, C. Johnson, T. Koretsune, J. Ibañez-Azpiroz, H. Lee, J.-M. Lihm, D. Marchand, A. Marrazzo, Y. Mokrousov, J. I. Mustafa, Y. Nohara, Y. Nomura, L. Paulatto, S. Poncé, T. Ponweiser, J. Qiao, F. Thöle, S. S. Tsirkin, M. Wierzbowska, N. Marzari, D. Vanderbilt, I. Souza, A. A. Mostofi, and J. R. Yates, Wannier90 as a community code: new features and applications, *J. Phys.: Condens. Matter* **32**, 165902 (2020).
- [40] F. Aryasetiawan, M. Imada, A. Georges, G. Kotliar, S. Biermann, and A. I. Lichtenstein, Frequency-dependent local interactions and low-energy effective models from electronic structure calculations, *Phys. Rev. B* **70**, 195104 (2004).
- [41] M. Bieniek, K. Sadecka, L. Szulakowska, and P. Hawrylak, Theory of Excitons in Atomically Thin Semiconductors: Tight-Binding Approach, *Nanomaterials* **12**, 1582 (2022).
- [42] A. C. Dias, J. F. Silveira, and F. Qu, WanTiBEXOS: A Wannier based Tight Binding code for electronic band structure, excitonic and optoelectronic properties of solids, *Comp. Phys. Commun.* **285**, 108636 (2023).
- [43] M. Rohlfing and S. G. Louie, Electron-hole excitations and optical spectra from first principles, *Phys. Rev. B* **62**, 4927 (2000).
- [44] E. Perfetto and G. Stefanucci, Real-Time *GW* -Ehrenfest-Fan-Migdal Method for Nonequilibrium 2D Materials, *Nano Lett.* **23**, 7029 (2023).
- [45] M. Lindberg and S. W. Koch, Effective Bloch equations for semiconductors, *Phys. Rev. B* **38**, 3342 (1988).
- [46] G. Stefanucci and E. Perfetto, Semiconductor electron-phonon equations: A rung above Boltzmann in the many-body ladder, *SciPost Phys.* **16**, 073 (2024).
- [47] S. Mocatti, G. Marini, G. Volpato, P. Cudazzo, and M. Calandra, Nonequilibrium Photocarrier and Phonon Dynamics from First Principles: a Unified Treatment of Carrier-Carrier, Carrier-Phonon, and Phonon-Phonon Scattering (2025).
- [48] G. Stefanucci and E. Perfetto, Unified first-principles formula for time-resolved arpes spectra of coherent and incoherent excitons (2026), arXiv:2601.16786 [cond-mat.mtrl-sci].
- [49] M. Schüler and M. A. Sentef, Theory of subcycle time-resolved photoemission: Application to terahertz photodressing in graphene, *Journal of Electron Spectroscopy and Related Phenomena* **253**, 147121 (2021).
- [50] C. Bao, M. Schüler, T. Xiao, F. Wang, H. Zhong, T. Lin, X. Cai, T. Sheng, X. Tang, H. Zhang, P. Yu, Z. Sun, W. Duan, and S. Zhou, Manipulating the symmetry of photon-dressed electronic states, *Nature Communications* **15**, 10535 (2024).
- [51] C. F. Klingshirn, *Semiconductor Optics*, 4th ed. (Springer Berlin Heidelberg, Berlin, Heidelberg, 2012) pp. 491–597, chaps. 19–21.
- [52] G. Kremer, M. Rumo, C. Yue, A. Pulkkinen, C. W. Nicholson, T. Jaouen, F. O. von Rohr, P. Werner, and C. Monney, Ultrafast dynamics of the surface photovoltage in potassium-doped black phosphorus, *Physical Review B* **104**, 035125 (2021).
- [53] Z. Chen, J. Dong, E. Papalazarou, M. Marsi, C. Giorgetti, Z. Zhang, B. Tian, J.-P. Rueff, A. Taleb-Ibrahimi, and L. Perfetti, Band Gap Renormalization, Carrier Multiplication, and Stark Broadening in Photoexcited Black Phosphorus, *Nano Letters* **19**, 488 (2019).
- [54] H. Hedayat, A. Ceraso, G. Soavi, S. Akhavan, A. Cadore, C. Dallera, G. Cerullo, A. C. Ferrari, and E. Carpane, Non-equilibrium band broadening, gap renormalization and band inversion in black phosphorus, *2D Materials* **8**, 025020 (2021).
- [55] S. Roth, A. Crepaldi, M. Puppini, G. Gatti, D. Bugini, I. Grimaldi, T. R. Barrilot, C. A. Arrell, F. Frassetto, L. Polletto, M. Chergui, A. Marini, and M. Grioni, Photocarrier-induced band-gap renormalization and ultrafast charge dynamics in black phosphorus, *2D Materials* **6**, 031001 (2019).
- [56] D. Sangalli, E. Perfetto, G. Stefanucci, and A. Marini, An ab-initio approach to describe coherent and non-coherent exciton dynamics, *Eur. Phys. J. B* **91**, 171 (2018).
- [57] V. Gosetti, J. Cervantes-Villanueva, S. Mor, D. Sangalli, A. Garcia-Cristobal, A. Molina-Sanchez, V. Agekyan, M. Tuniz, D. Puntel, W. Bronsch, F. Cilento, and S. Pagliara, Unveiling the exciton formation in time, energy and momentum domain in layered van der Waals semiconductors, *Progress in Surface Science* **100**, 100777 (2025).
- [58] C. Trovatello, F. Katsch, N. J. Borys, M. Selig, K. Yao, R. Borrego-Varillas, F. Scotognella, I. Kriegel, A. Yan, A. Zettl, P. J. Schuck, A. Knorr, G. Cerullo, and S. D. Conte, The ultrafast onset of exciton formation in 2D semiconductors, *Nature Communications* **11**, 5277 (2020).
- [59] M. Fanciulli, D. Bresteau, J. Gaudin, S. Dong, R. Géneaux, T. Ruchon, O. Tcherbakoff, J. Minár, O. Heckmann, M. C. Richter, K. Hricovini, and S. Beaulieu, Ultrafast hidden spin polarization dynamics of bright and dark excitons in 2H-WSe₂, *Phys. Rev. Lett.* **131**, 066402 (2023).
- [60] J. Madéo, M. K. L. Man, C. Sahoo, M. Campbell, V. Pareek, E. L. Wong, A. Al-Mahboob, N. S. Chan, A. Karmakar, B. M. K. Mariserla, X. Li, T. F. Heinz, T. Cao, and K. M. Dani, Directly visualizing the momentum-forbidden dark excitons and their dynamics in atomically thin semiconductors, *Science* **370**, 1199 (2020).
- [61] D. Wang, P. Yi, L. Wang, L. Zhang, H. Li, M. Lu, X. Xie, L. Huang, and W. Huang, Revisiting the Growth of Black Phosphorus in Sn-I Assisted Reactions, *Frontiers in Chemistry* **7**, 21 (2019).
- [62] J. Faure, J. Mauchain, E. Papalazarou, W. Yan, J. Pinon, M. Marsi, and L. Perfetti, Full characterization and optimization of a femtosecond ultraviolet laser source for time and angle-resolved photoemission on solid surfaces, *Review of Scientific Instruments* **83**, 043109 (2012).
- [63] D. Wortmann, G. Michalicek, R. Hilgers, A. Neukirchen, H. Janssen, U. Grytsiuk, J. Broeder, and C.-R. Gerhorst, *Fleur* (2023).
- [64] L. Hedin, New Method for Calculating the One-Particle Green's Function with Application to the Electron-Gas Problem, *Phys. Rev.* **139**, A796 (1965).
- [65] G. Pizzi, V. Vitale, R. Arita, S. Blügel, F. Freimuth, G. Géranton, M. Gibertini, D. Gresch, C. Johnson, T. Koretsune, J. Ibañez-Azpiroz, H. Lee, J.-M. Lihm, D. Marchand, A. Marrazzo, Y. Mokrousov, J. I. Mustafa, Y. Nohara, Y. Nomura, L. Paulatto, S. Poncé, T. Ponweiser, J. Qiao, F. Thöle, S. S. Tsirkin, M. Wierzbowska, N. Marzari, D. Vanderbilt, I. Souza, A. A. Mostofi, and J. R. Yates, Wannier90 as a community code: new features and applications, *Journal of Physics: Condensed*

Matter **32**, 165902 (2020).

- [66] C. Friedrich, S. Blügel, and A. Schindlmayr, Efficient implementation of the GW approximation within the all-electron FLAPW method, *Phys. Rev. B* **81**, 125102 (2010).
- [67] F. Aryasetiawan, M. Imada, A. Georges, G. Kotliar, S. Biermann, and A. I. Lichtenstein, Frequency-dependent local interactions and low-energy effective models from electronic structure calculations, *Phys. Rev. B* **70**, 195104 (2004).
- [68] G. Cappellini, R. Del Sole, L. Reining, and F. Bechstedt, Model dielectric function for semiconductors, *Phys. Rev. B* **47**, 9892 (1993).
- [69] H. Zabel, Phonons in layered compounds, *Journal of Physics: Condensed Matter* **13**, 7679 (2001).
- [70] A. Politano, A. R. Marino, D. Campi, D. Farías, R. Miranda, and G. Chiarello, Elastic properties of a macroscopic graphene sample from phonon dispersion measurements, *Carbon* **50**, 4903 (2012).
- [71] Y. Fujii, Y. Akahama, S. Endo, S. Narita, Y. Yamada, and G. Shirane, Inelastic neutron scattering study of acoustic phonons of black phosphorus, *Solid State Communications* **44**, 579 (1982).
- [72] G. Qin, Q.-B. Yan, Z. Qin, S.-Y. Yue, M. Hu, and G. Su, Anisotropic intrinsic lattice thermal conductivity of phosphorene from first principles, *Phys. Chem. Chem. Phys.* **17**, 4854 (2015).
- [73] L. Zhu, G. Zhang, and B. Li, Coexistence of size-dependent and size-independent thermal conductivities in phosphorene, *Phys. Rev. B* **90**, 214302 (2014).
- [74] J. R. Yates, X. Wang, D. Vanderbilt, and I. Souza, Spectral and Fermi surface properties from Wannier interpolation, *Phys. Rev. B* **75**, 195121 (2007).
- [75] W. Li, J. Carrete, N. A. Katcho, and N. Mingo, Shengbte: A solver of the Boltzmann transport equation for phonons, *Computer Physics Communications* **185**, 1747 (2014).
- [76] L. Miaja-Avila, C. Lei, M. Aeschlimann, J. L. Gland, M. M. Murnane, H. C. Kapteyn, and G. Saathoff, Laser-Assisted Photoelectric Effect from Surfaces, *Phys. Rev. Lett.* **97**, 113604 (2006).
- [77] F. Mahmood, C.-K. Chan, Z. Alpichshev, D. Gardner, Y. Lee, P. A. Lee, and N. Gedik, Selective scattering between Floquet–Bloch and Volkov states in a topological insulator, *Nature Physics* **12**, 306 (2016).
- [78] M. Schüler and S. Beaulieu, Probing topological Floquet states in WSe₂ using circular dichroism in time- and angle-resolved photoemission spectroscopy, *Communications Physics* **5**, 164 (2022).
- [79] G. Saathoff, L. Miaja-Avila, M. Aeschlimann, M. M. Murnane, and H. C. Kapteyn, Laser-assisted photoemission from surfaces, *Physical Review A* **77**, 022903 (2008).

AUTHOR CONTRIBUTIONS STATEMENT

C.M., M.S. and G.K. designed the research. G.K., J.M., A.M., F.C. and M.R. carried out the experiments and measurements. V.C. and P.W. performed the DFT calculations. F.O.v.R. and M. B. performed sample growth and initial characterization. G.K., J.M. and A.M. analyzed the data with help from all the authors. J.F.P.M. and M.S. developed the quantum-kinetic theoretical model and performed the simulations. J.F.P.M., J.M., C.M., M.S. and G.K. wrote the paper, with input from all authors. All authors reviewed the manuscript.

ACKNOWLEDGMENTS

This project was supported by Swiss National Science Foundation Grant No. 10000782 and No. P00P2_170597. Skillful technical assistance was provided by J. L. Andrey, M. Andrey, F. Bourqui, and B. Hediger.

Supplementary Material for “Ultrafast dynamics of excitons in black phosphorus”

BAND STRUCTURE AND WANNIER-BLOCH BASIS

We performed density functional theory (DFT) calculations using the FLEUR full-potential all-electron code [63]. We used a $12 \times 12 \times 8$ \mathbf{k} -grid for the calculations. The atomic positions and lattice parameters for the orthorhombic lattice are given in Table I. On top of the DFT calculations, we performed a one-shot G^0W^0 calculation [64] to obtain the self-energy $\Sigma_\alpha(\mathbf{k})$, from

a	b	c
3.331 Å	4.585 Å	10.989 Å

TABLE I. Lattice parameters (in Å) for the relaxed structure of bulk black Phosphorus.

which the quasi-particle energies ε_α^{QP} are computed. The quasi-particle energies are then obtained by solving the quasi-particle equation

$$\varepsilon_\alpha^{QP}(\mathbf{k}) = \varepsilon_\alpha(\mathbf{k}) - V_\alpha^{xc}(\mathbf{k}) + \Re \{ \Sigma_\alpha(\mathbf{k}, \varepsilon_\alpha^{QP}(\mathbf{k})) \}, \quad (\text{S1})$$

where $\varepsilon_\alpha(\mathbf{k})$ and $V_\alpha^{xc}(\mathbf{k})$ are the Kohn-Sham eigenvalues and the exchange-correlation potential from the DFT calculation, respectively. The resulting quasi-particle Hamiltonian is expressed in the basis of projective Wannier functions $\phi_j(\mathbf{r} - \mathbf{R})$ using the Wannier90 code [65]. We include the s - and p -orbitals of Phosphorus. The band structure of the system is shown in Fig. S1. We shifted the bands such that the valence band maximum (VBM) is located at $\varepsilon_{\text{VBM}} = 0$. Because the G_0W_0 bands predict a too large band gap compared to the experimental value, we applied a scissor operator to fix, $E_{\text{gap}} = 0.31$ eV. In the equations and discussion listed below, we have omitted the labels QP in the quasi-particle states.

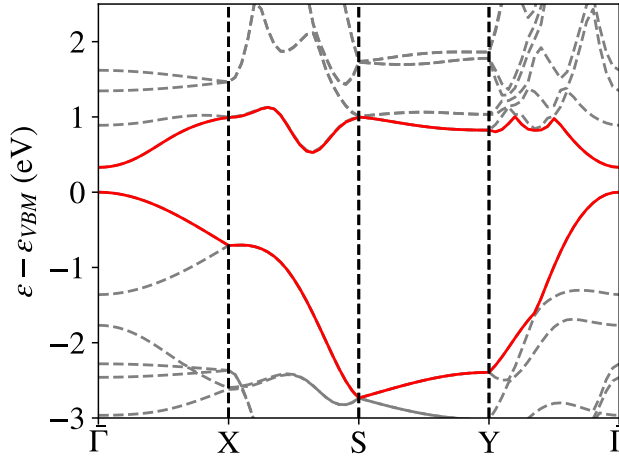


FIG. S1. **Band Structure of Bulk Black Phosphorus:** G^0W^0 quasi-particle band structure (gray dashed lines). The two red lines show the top valence and bottom conduction band, respectively.

COULOMB INTERACTIONS

As the next step, we performed constrained random-phase approximation (cRPA) calculations to obtain the Coulomb matrix elements in the Wannier basis using the SPEX code [66, 67], with the target space being the valence and conduction bands. Keeping only the density-density matrix elements due to the localized nature of the Wannier functions and the static approximation,

the interaction Hamiltonian takes the form

$$\hat{H}_{int} = \frac{1}{2} \sum_{\mathbf{R}\mathbf{R}'} \sum_{ij} U_{ij}(\mathbf{R} - \mathbf{R}') \hat{n}_{i\mathbf{R}} \hat{n}_{j\mathbf{R}'}, \quad (\text{S2})$$

where $\hat{n}_{i\mathbf{R}} = \hat{c}_{i\mathbf{R}}^\dagger \hat{c}_{i\mathbf{R}}$ is the density operator for orbital i on lattice site \mathbf{R} .

The cRPA calculations have been performed on a $N = 32 \times 32 \times 32$ supercell, which is sufficient to accurately describe the short-range part of $U_{ij}(\mathbf{R})$. To capture the asymptotic behavior of the effective bare Coulomb interaction, we have fitted it to a function of the shape

$$U_{ij}(\mathbf{R}) \propto \frac{v_{ij}}{|\mathbf{R} + (\mathbf{r}_i - \mathbf{r}_j)|}. \quad (\text{S3})$$

From the representation in the Wannier basis of the effective bare Coulomb interaction, we compute Coulomb interaction in the band basis by

$$V_{\alpha\beta\gamma\sigma}(\mathbf{k}, \mathbf{k}', \mathbf{Q}) = \sum_{ij} U_{ij}(\mathbf{Q}) C_{i\alpha}^*(\mathbf{k}) C_{j\beta}^*(\mathbf{k}') C_{j\alpha}(\mathbf{k}' + \mathbf{Q}) C_{i\beta}(\mathbf{k} - \mathbf{Q}). \quad (\text{S4})$$

For computing the screened interaction, we performed RPA calculations. However, since the convergence is slow and computationally expensive, we used the information from the RPA calculation for the short-range part, but used a model dielectric function $\epsilon(\mathbf{Q})$ (we only consider static screening) for the long-range interaction. The long-range part screened interaction in Wannier basis is then defined by

$$W_{ij}(\mathbf{Q}) = \epsilon^{-1}(\mathbf{Q}, \omega = 0) U_{ij}(\mathbf{Q}). \quad (\text{S5})$$

For bulk semiconductors, a well-used model was proposed in Ref. [68] where the static dielectric function takes the form

$$\epsilon(\mathbf{Q}) = 1 + \frac{1}{\frac{1}{\epsilon(\mathbf{Q}=0)-1} + \alpha \frac{Q^2}{q_{TF}^2} + \frac{Q^4}{4\omega_p^2}}. \quad (\text{S6})$$

Here, $q_{TF} = 2(3\bar{n}/\pi)^{1/6}$ and $\omega_p = \sqrt{4\pi\bar{n}}$ (where $\bar{n} = n/V$ is the average density of electrons) are the Thomas-Fermi wave vector and the plasma frequency, respectively. For this case, the number of electrons in the system is 48, and the volume V is given by the product of the lattice vectors in Table I. The parameter α is set to 1.563, which is the averaged value extracted from other materials. Small variations of it do not drastically affect the RPA results [68]. The value we used for the macroscopic dielectric constant is $\epsilon(\mathbf{Q} = 0) = 6.36$, obtained by minimizing the error of the screened interaction with the RPA calculation in the short range. By using the models described in Eq. (S3) and Eq. (S5), we ensure the asymptotic behavior of the interactions.

In Fig. S2, the short- and long-range screened interactions are shown with black and gray dots, respectively. The red dots correspond to the screened interaction used in the following sections, which is obtained by merging the short- and long-range ones. For distances smaller than their intersection, we used the short-range fitting, and for distances larger than the intersection point, we used the long-range interaction.

BETHE-SALPETER EQUATION (BSE)

After computing the band structure, the bare Coulomb, and the screened interaction, we proceed to computing the excitons properties. The exciton state can be written as

$$|\Psi^{\lambda, \mathbf{Q}}\rangle = \frac{1}{N_k} \sum_{\mathbf{k}} \sum_{\zeta\nu} \Lambda_{\nu\zeta}^{\lambda, \mathbf{Q}}(\mathbf{k}) \hat{c}_{\nu, \mathbf{k}+\mathbf{Q}}^\dagger \hat{v}_{\zeta, \mathbf{k}} |\Psi_0\rangle, \quad (\text{S7})$$

where $\Lambda_{\nu\zeta}^{\lambda, \mathbf{Q}}(\mathbf{k})$ is the exciton wave function, whose quantum numbers we label by λ . The operators $\hat{v}_{\zeta, \mathbf{k}}$ remove an electron in the valence (ζ) states, and the operators $\hat{c}_{\nu, \mathbf{k}+\mathbf{Q}}^\dagger$ create an electron in the conduction (ν) states with momentum $\mathbf{k} + \mathbf{Q}$. To obtain the exciton wave function, we solved the BSE, which reads as

$$(E_\lambda(\mathbf{Q}) - \epsilon_C + \epsilon_V) \Lambda_{C\nu}^{\lambda, \mathbf{Q}}(\mathbf{k}) = - \sum_{C'\nu'} [W_{C\nu'V C'} - V_{C\nu' C'V}] \Lambda_{C'\nu'}^{\lambda, \mathbf{Q}}(\mathbf{k}'), \quad (\text{S8})$$

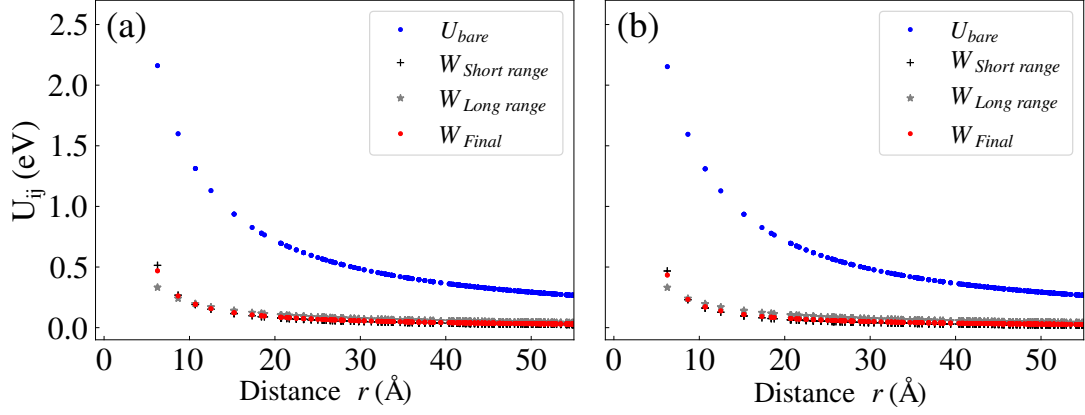


FIG. S2. **Distance Dependence of the Effective Interactions:** In blue, the static nonlocal cRPA interaction $U_{ij}(\mathbf{R})$ fitted to the model function given in Eq. (S3). In black and gray, the short- and long-range screened Coulomb interactions. The red dots are the screened interactions obtained by merging the short- and long-range components. Panels (a) and (b) show the interband interactions between Wannier orbitals with indexes $i, j = 19$ and $i, j = 20$, respectively, dominated by the p_z orbitals.

where the index C (C') corresponds to the conduction state with momentum $\mathbf{k} + \mathbf{Q}$ ($\mathbf{k}' + \mathbf{Q}$). The index V (V') corresponds to the valence state with momentum \mathbf{k} (\mathbf{k}'). In our case, we are just taking into account one single valence and conduction state. From now on we omit the labels C and V in the exciton wave function $[\Lambda^{\lambda, \mathbf{Q}}(\mathbf{k})]$. The corresponding dispersion energy for the ground-state excitons ($E_{\lambda=0}$) is shown in Fig. S3 along the Q_x , Q_y , and Q_z directions. Note that the band gap of the band dispersion energy does not change the exciton dispersion energy, only the binding energy. Therefore, we plotted it by setting the zero energy to the coherent exciton energy. In this study we have focused on the ground state exciton ($\lambda = 0$), thus in the analysis we have skipped these indexes.

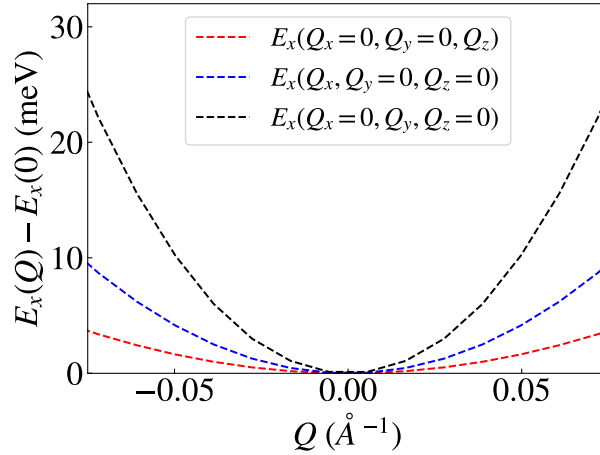


FIG. S3. **Exciton Dispersion Energy:** Ground state dispersion energy E_x along the different directions Q_x , Q_y , and Q_z .

In Fig. S4, we show the exciton wave functions by fixing Q_x and Q_z to zero and displaying different values of Q_y . The wave function is symmetric under changes of sign in the momentum, i.e., $\Lambda^{\mathbf{Q}}(\mathbf{k}) = \Lambda^{-\mathbf{Q}}(\mathbf{k})$. At this step, we obtained the exciton wave function for a discrete grid of points \mathbf{Q} , not far from $\bar{\Gamma}$, and fitted it using a function with the shape

$$\left| \Lambda^{\mathbf{Q}}(\mathbf{k}) \right|^2 = C \prod_{i \in \{x, y, z\}} (1 + a_i Q_i) e^{-(Q_i - Q_i^0)^2 / \sigma_i^2} \left| \Lambda^{\mathbf{Q}=0}(\mathbf{k}) \right|^2, \quad (\text{S9})$$

where C and a_i are the parameters that modulate the amplitude, Q_i^0 is the position of the maximum of the wave function, and σ_i^2 is the width of the Gaussian distribution.

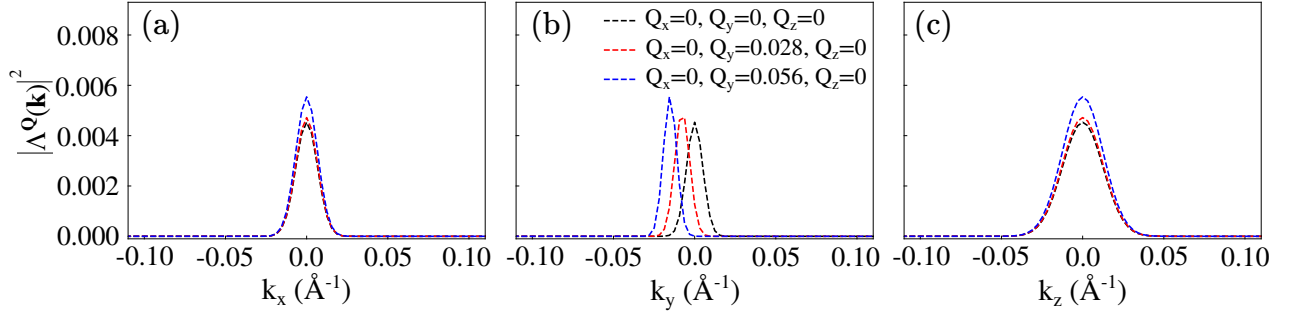


FIG. S4. Exciton's density for different values of \mathbf{Q} , (a) along k_x and fixing $k_y = k_z = 0$, (b) along k_y and fixing $k_x = k_z = 0$, (c) along k_z and fixing $k_x = k_y = 0$

QUANTUM BOLTZMANN AND EXCITON BLOCH EQUATIONS

To characterize the scattering dynamics and momentum redistribution of photo-excited carriers, we model the temporal evolution of exciton populations using a density matrix approach. We define a reduced basis consisting of three primary states: the initial many-body ground state (represented by the occupied valence band at the Γ point) $|\Psi_0\rangle$, the optically generated coherent exciton population at the center of mass momentum $\mathbf{Q} = 0$ (the "bright" exciton state $|\Psi_{\mathbf{Q}=0}^{\text{exc}}\rangle$), and the manifold of incoherent exciton populations at $\mathbf{Q} \neq 0$ ($|\Psi_{\mathbf{Q}\neq 0}^{\text{exc}}\rangle$). The dynamics are governed by the exciton Bloch equations [12], here simplified for the low-density limit. They follow the same spirit as the semiconductor Bloch equations, where the scattering is described by Markovian Boltzmann-like terms for the incoherent populations.

The evolution of the exciton density matrix, $\rho^{\text{exc}}(t)$, is described by the master equation

$$\frac{d}{dt}\rho^{\text{exc}}(t) = -i[\hat{H}^{\text{exc}}, \rho^{\text{exc}}(t)] + \mathcal{S}^{\text{exc}}(t), \quad (\text{S10})$$

where the ground state $|\Psi_0\rangle$ and the bright exciton state $|\Psi_{\mathbf{Q}=0}^{\text{exc}}\rangle$ are coupled by the Hamiltonian term

$$\langle \Psi_0 | \hat{H}_{\text{exc}}(t) | \Psi_{\mathbf{Q}=0}^{\text{exc}} \rangle = -\mathbf{E}(t) \cdot \mathbf{M}_x^{\text{dip}}. \quad (\text{S11})$$

The pump excitation is provided by a Gaussian electric pulse $\mathbf{E}(t) = E_0 \boldsymbol{\epsilon} e^{-(t-t_0)^2/2\sigma^2} \cos[\omega_{\text{pump}}(t-t_0)]$. We employ a pulse with a full-width at half-maximum (FWHM) of 226.27 fs, a resonant frequency that matches the exciton resonance energy and a field amplitude of $E^{(0)} = 1.5$ kV/cm, which will be explained in detail in the next section. The polarization vector is set to $\boldsymbol{\epsilon} = (0, 0.2912, 0)$, which has been computed using the Fresnel transmission coefficients. The transition matrix elements, \mathbf{M}_x , are calculated in the velocity gauge by evaluating the velocity matrix between the valence and conduction states weighted by the exciton wave function

$$\mathbf{M}_x^{\text{vel}} = \frac{1}{\sqrt{N_k}} \sum_{\mathbf{k}} \Lambda^{\mathbf{Q}=0}(\mathbf{k}) \mathbf{v}_{CV}(\mathbf{k}), \quad (\text{S12})$$

where $\mathbf{v}_{CV}(\mathbf{k}) = -i[\epsilon_C(\mathbf{k}) - \epsilon_V(\mathbf{k})] \mathbf{A}_{CV}(\mathbf{k})$, here $\mathbf{A}_{CV}(\mathbf{k})$ is the Berry connection and then convert it from the velocity to the dipole gauge.

Coherent excitons at $\mathbf{Q} = 0$ scatter to finite momenta $\mathbf{Q} \neq 0$ via interactions with the phonon bath. This process facilitates energy exchange between the electronic system and the lattice. The momentum-dependent scattering rates, $\Gamma_{\mathbf{Q} \rightarrow \mathbf{Q}'}$, are given by:

$$\Gamma_{\mathbf{Q} \rightarrow \mathbf{Q}'}(T) = 2\pi\gamma^2 |\mathbf{Q} - \mathbf{Q}'| \left[n_{\text{ph}}(\mathbf{Q} - \mathbf{Q}', T) \delta(E_x(\mathbf{Q}) - E_x(\mathbf{Q}') + \omega_{\text{ph}}(\mathbf{Q}' - \mathbf{Q})) \right. \\ \left. + (n_{\text{ph}}(\mathbf{Q} - \mathbf{Q}', T) + 1) \delta(E_x(\mathbf{Q}) - E_x(\mathbf{Q}') - \omega_{\text{ph}}(\mathbf{Q}' - \mathbf{Q})) \right]. \quad (\text{S13})$$

Here, ω_{ph} represents the phonon dispersion. In layered compounds, acoustic modes typically exhibit a parabolic dispersion at small wavenumbers; however, finite shear interactions between layers can result in a non-zero slope at $\mathbf{Q} = 0$. Consequently, we

approximate the acoustic dispersion near the $\bar{\Gamma}$ point linearly as

$$\omega_{\text{ph}}^2(\mathbf{Q}) = \sum_{i \in \{x,y,z\}} v_i^2 Q_i^2, \quad (\text{S14})$$

where $v_i = \partial_{Q_i} \omega_{\text{ph}}(\mathbf{Q})$ is the group velocity [69, 70]. We adopt group velocities from previous experimental reports [71–73]. Our model considers only acoustic phonon dispersions, as optical phonons in this system possess energies significantly exceeding the exciton dispersion scale and do not contribute to the scattering channels considered here.

The phonon population, $n_{\text{ph}}(\mathbf{Q}, T)$, follows the Bose-Einstein statistics. In Eq. (S10), the relaxation and dephasing take the form of $S^{\text{exc}} = -2 \sum_{\mathbf{Q} \neq 0} \Gamma_{\mathbf{0} \rightarrow \mathbf{Q}}$.

To ensure the conservation in the density of particles of the momentum grid, we regularize the Dirac delta functions in Eq. (S13) using a Gaussian approximation: $\delta_{\sigma}(\omega) = \frac{1}{\sqrt{2\pi}\sigma} e^{-\omega^2/(2\sigma^2)}$. To avoid the arbitrary tuning of results, we implement a state-dependent broadening width

$$\sigma_{\mathbf{Q}} = a \left| \frac{\partial E(\mathbf{Q})}{\partial \mathbf{Q}} \right| \Delta Q. \quad (\text{S15})$$

This approach ensures that the broadening remains proportional to the local energy gradient and grid spacing, ΔQ , thereby guaranteeing a consistent convergence toward the ideal Dirac delta limit as $\Delta Q \rightarrow 0$ [74, 75].

CONNECTING THEORY AND EXPERIMENTS

To connect the theoretical formalism with the experimental results, we follow a systematic procedure to determine the model parameters. This section outlines the formalism for the signal components, the simulation integration, and the extraction of the parameters used: α (LAPE scaling), $E^{(0)}$ (theory electric field amplitude), and γ (exciton-phonon coupling strength).

Formalism and Simulation Details

The total trARPES intensity is modeled as the sum of the excitonic signal and the Laser-Assisted Photoemission Effect (LAPE) contribution. The LAPE signal represents a coherent phenomenon where the pump pulse dresses electronic states, appearing as replicas of the valence band shifted by the pump photon energy [76–78]. It is defined as

$$I_{\text{LAPE}}(\mathbf{k}_{\parallel}, \omega, \tau) = \alpha f^2(\tau) \int dk_z F(k_z - p_{\perp}) |M_v(\mathbf{k}, p_{\perp})|^2 \delta(\epsilon_v(\mathbf{k}) + \omega_{\text{pump}} - \omega), \quad (\text{S16})$$

where $f(\tau)$ is the envelope of the electric field (making f^2 the intensity profile), ω_{pump} is the pump frequency and α is a scaling parameter.

Parameter Determination Procedure

The parameters are extracted from the experimental data by following the steps:

- **Field Strength ($E^{(0)}$):** We first examine the steady state at late times ($t \rightarrow \infty$) after the pump pulse has finished. In this regime, the LAPE signal vanishes. To compare with the experimental distributions, we compute the energy distribution curves (EDC) by integrating the simulated intensity over a momentum range of $[-0.05, 0.05] \text{ \AA}^{-1}$ near $\bar{\Gamma}$. We set the field strength to $E^{(0)} = 1.5 \text{ kV/cm}$ to match the intensity of the exciton peak between the simulation and experiment in the EDC. This value serves as an effective internal field strength.
- **LAPE Amplitude (α) and ROI Analysis:** The parameter α is adjusted by analyzing the "red box" ROI (way below the exciton's binding energy). This region is dominated by LAPE, which is symmetric in time around $\tau = 0$. By matching this ROI, we scale it to be $\alpha = 7.0 \times 10^{-4}$. The small remaining asymmetry and signal at later times in this region are then used to confirm the minor contribution of the exciton signal in this domain.
- **Effective Coupling Strength (γ):** Finally, the exciton-phonon coupling strength γ is determined by fitting the dynamics in the "green box" and "blue box" ROI. Unlike the LAPE signal, the excitonic signal is asymmetric and exhibits a delayed rise time as bright excitons at $Q = 0$ scatter into dark states at $Q \neq 0$. By fitting this rise time and the relative amplitudes across the ROI [Fig. 2b-d], we obtain a unique choice for $\gamma \simeq 2.5 \times 10^{-4}$ a.u.

LASER ASSISTED PHOTOEMISSION EFFECT

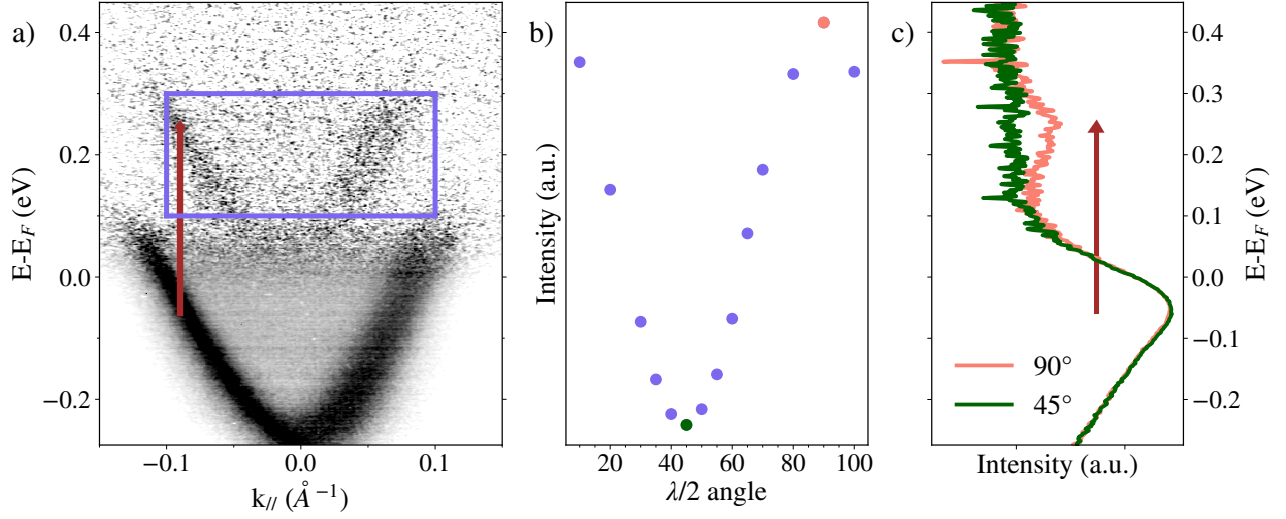


FIG. S5. **Experimental Measurement of LAPE on Bi_2Se_3 :** (a) Pump-probe ARPES spectrum acquired using a p -polarized pump with $\hbar\omega_p = 0.31$ eV, showing the replica of the Dirac cone shifted by the photon energy. (b) Integrated signal in the blue ROI of (a) as a function of wave plate angle. (c) EDCs on pump-probe ARPES spectra using s -polarized (green) and p -polarized (orange) pump photons.

In pump-probe ARPES, the laser assisted photoemission effect (LAPE) emerges as a dressing of the final photoelectron state with infrared radiation when using p -polarized pump photons [77, 79]. It manifests as replica of the occupied states, shifted by the pump photon energy $\hbar\omega_p$, shown in Fig. S5(a). To avoid interference with exciton signature measurements, the pump photons are set to s -polarization using a $\lambda/2$ wave plate. The $\lambda/2$ wave plate was calibrated at pump photon energies of $\hbar\omega_p = 0.31$ eV and $\hbar\omega_p = 0.41$ eV by performing pump-probe ARPES measurements on the topological insulator Bi_2Se_3 . By selecting a ROI where the replica is expected and integrating its signal across different wave plate configurations, the LAPE intensity is quantified as a function of the $\lambda/2$ angle. The orange EDC in Fig. S5(c) shows the maximal LAPE configuration, characterized by a replica band shifted by 0.31 eV above the main peak. The absence of residual signal in the unoccupied states for the green EDC indicates that the corresponding wave plate setting yields pure s -polarization. The same procedure was performed for 0.41 eV pump photons with the appropriate $\lambda/2$ wave plate.